

Data Repository 1: Uncertainty analysis of the average PoR velocity field

We present the SCEC 3.0 velocity field in the spherical pole of rotation (PoR) coordinate system. Because the transformed velocity vectors and their uncertainties depend on the PoR location, it is important to consider the role various pole estimates. Here we use four recent GPS-determined Pa-NA PoR estimates (Table DR1). Although each of the four studies report very high precision levels, as shown by their very small uncertainty ellipses, their locations are spread over a wide area (Figure 1c).

To calculate velocity uncertainties, we first transform the velocity field according to each of the four GPS-based poles (1-4 in Table DR1), thereby obtaining four sets of dimensionless velocity vectors and uncertainty values. To illustrate this point we provide example of site HAPY (Figure DR1, left arrows), where the four transformed vectors are of a similar orientation but with slightly different magnitude reflecting mainly changes in the longitudinal component. The velocity differences result from the variable distance between GPS-determined poles locations and location of the geodetic measurements in southern California (Figure 1). In order to account for the variations between the four transformed vectors, we calculate an average vector and corresponding uncertainties (Figure DR1, right arrows). The uncertainty calculation considers both the average uncertainty for each of the four vectors and the value difference between the average vector and the four transformed vectors.

References

- Beavan, J., Tregoning, P., Bevis, M., Kato, T., and Meertens, C., 2002, Motion and rigidity of the Pacific Plate and implications for plate boundary deformation: *Journal of Geophysical Research-Solid Earth*, v. 107.
- DeMets, C., Gordon, R.G., Argus, D.F., and Stein, S., 1994, Effect Of Recent Revisions To The Geomagnetic Reversal Time-Scale On Estimates Of Current Plate Motions: *Geophysical Research Letters*, v. 21, p. 2191-2194.
- Gonzalez-Garcia, J.J., Prawirodirdjo, L., Bock, Y., and Agnew, D., 2003, Guadalupe Island, Mexico as a new constraint for Pacific plate motion: *Geophysical Research Letters*, v. 30.
- Prawirodirdjo, L., and Bock, Y., 2004, Instantaneous global plate motion model from 12 years of continuous GPS observations: *Journal of Geophysical Research-Solid Earth*, v. 109.
- Sella, G.F., Dixon, T.H., and Mao, A.L., 2002, REVEL: A model for Recent plate velocities from space geodesy: *Journal of Geophysical Research-Solid Earth*, v. 107.

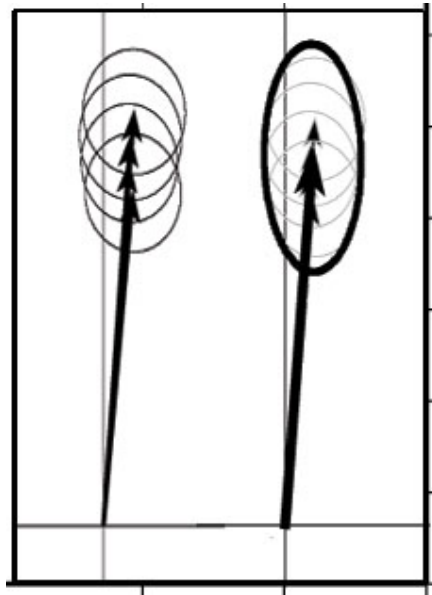


Figure DR1. Example of the statistical analysis used to calculate the normalized velocity vector. Left: Normalized velocity estimates at site HAPY according to the four GPS-determined PoRs (Table S1). Right: Normalized velocity calculated according to the averaged PoR and the statistical analysis that considers the magnitudes of the four vectors.

TABLE DR1: ESTIMATES OF THE PACIFIC-NORTH AMERICA POLE OF ROTATION

No.*	Euler Vector	Lat. (°N)	Lon. (°E)	Rate (°/Myr)	Pole Error Ellipse		
					σ_{\max}^{\dagger}	σ_{\min}^{\dagger}	Az. §
1	(Gonzalez-Garcia et al., 2003)	49.89	282.99	0.766 ± 0.007	0.24	0.17	70
2	(Prawirodirdjo and Bock, 2004)	50.16	284.17	0.766 ± 0.006	0.13	0.06	36
3	(Beavan et al., 2002)	50.26	284.96	0.773 ± 0.005	0.41	0.17	94
4	(Sella et al., 2002), REVEL-2000	50.38	287.89	0.755 ± 0.004	0.6	0.4	101
5	(DeMets et al., 1994) NUVEL-1A	48.7	281.8	0.75 ± 0.01	1.3	1.2	119
6	This study – Average (1-4)	50.17	285.00	0.765 ± 0.009	2.8	0.6	75

*Reference number for pole presentation in Figure 1c.

† Two-dimensional 1-sigma lengths in degrees of the semi-major σ_{\max} and semi-minor σ_{\min} of the pole error ellipse.

§ The azimuth (degrees) is the clockwise angle between north and the semi-major ellipse axis.

Data Repository 2: Viscoelastic modeling

The viscoelastic model used for analysis of the SCEC 3.0 velocity field accounts for the three dominant processes governing crustal movements in the period between large earthquakes: elastic strain accumulation of the crust, elastic coseismic displacements, and post-seismic viscous relaxation of the underlying mantle. The model consists of an elastic plate overlying a Maxwell viscoelastic half-space, with faults embedded within the elastic plate that extend from the surface to a prescribed locking depth (e.g., Savage and Prescott (1978)). Fault slip rate, historical/pre-historical earthquake sequence, and recurrence intervals are used to establish the magnitude of coseismic slip events. Transient deformation follows each earthquake due to viscoelastic flow in the underlying half-space.

The viscoelastic model we employ is based on semi-analytic solutions, derived in the Fourier domain, that provide the 3-D displacement response due to an arbitrary distribution of vector body forces (Smith and Sandwell, 2004). The restoring force of gravity is included to accurately model vertical deformation. The solution satisfies the zero-traction surface boundary condition and maintains stress and displacement continuity across the base of the plate. For simplicity, we ignore the effects of Earth's sphericity. We assume fixed values for the shear modulus $\mu = 24$ GPa, Young's modulus $E = 60$ GPa, elastic plate thickness $H = 65$ km, and viscosity $\eta = 3 \times 10^{18}$ Pa s (Smith and Sandwell, 2006). This complete fault model is used to efficiently explore the 3-D viscoelastic response of the upper mantle spanning the last 500 years of the San Andreas Fault System (SAFS) earthquake cycle in southern California.

Using hundreds of dislocations to represent complex geometry of the major faults of the SAFS, we model 24 fault segments spatially consistent with previous geologic and geodetic studies (Figure DR2). The model fault system is rotated about the Pa-Na pole of rotation (Data Repository 1) and model fault segments are embedded in a 1-km grid of 2048 elements along the SAFS and 1024 elements across the system. We employ published slip rates (Working Group on California Earthquake Probabilities, 1995) and apparent locking depth estimates (Smith and Sandwell, 2003) adjusted for viscoelastic effects (Smith and Sandwell, 2006) (Table DR2). Coseismic and postseismic deformation is modeled using 70 earthquake ruptures, compiled from both historical data and paleoseismic data (see Smith and Sandwell (2006) for a complete archive). It should also be noted that we include the

coseismic/postseismic response of both the 1992 $M_w = 7.3$ Landers earthquake and the 1999 $M_w = 7.1$ Hector Mine earthquake in the ECSZ. The resulting velocity field calculated by our viscoelastic model (Figures 3b and 3e) is very similar to the observed field.

Each of the fault segments is assigned a deep slip rate based on geodetic measurements, geologic offsets, and plate reconstructions; in some cases, slip rates were adjusted (± 5 mm/yr on average) in order to satisfy an assumed far-field velocity of 45 mm/yr. It should be noted that this far-field velocity assumption is lower than the estimated full North America-Pacific plate motion of 46-50 mm/yr (DeMets et al., 1994; Working Group on California Earthquake Probabilities, 1995, 1999) because we do not account for the entire network of active faults that also contribute to the overall plate velocity. This constant rate simplifies the model and provides a good fit to the geodetic data, except in the regions where misfit is expected due to omission of faults in this area. Following several initial rounds of modeling, we also adjusted slip rates on some model fault segments to match more recent slip rate estimates derived from geodetic analyses (e.g., Becker et al., 2004; Meade and Hager, 2005) and to also reflect the addition of several model faults in the ECSZ. These adjustments helped minimize the rms misfit along the San Bernardino, Mojave, and central SAF segments, with an 11% improvement to the fault-parallel rms misfit (1.98 mm/yr) and a 2% misfit improvement in the fault-perpendicular component (1.80 mm/yr). Several variations in slip-rate and locking depth scenarios were tested, however a simultaneous minimization of rms misfit of both fault-normal and fault-parallel velocity components proved challenging. For example, applying a more shallow locking depth to the Carrizo segment yielded a better fit to the fault-parallel velocity field (and also substantially reduced the negative misfit in this region (Figure 3c)), however doing so also produced an elevated misfit in the fault-normal velocity component in this region. Meade and Hager (2005) also report higher model misfits in this region, however their analysis was based on an elastic half-space model. In comparison, we calculate the effects of both an elastic model (i.e., no earthquakes) and the viscoelastic model discussed here and find a 10% reduction of fault-normal velocity misfit and a 6% reduction of the fault-parallel misfit when employing the viscoelastic model over an elastic model. It should also be noted that we experimented with variations in elastic plate thickness to best fit the SCEC velocity data and found that a thin plate (i.e., $H = 30$ km) increased the rms misfit by $\sim 20\%$ in both fault-

parallel and normal components. A more rigorous treatment of model fault parameters (i.e. least squares inversion) is necessary to establish further improvements to the data fit and this is certainly the focus of a future study. However, it should also be noted that our model does not include complex rheological variations (both laterally and with depth) (e.g., Malservisi et al., 2001), changes in local pore-pressure (e.g., Peltzer et al., 1996), or non-linear postseismic behavior (e.g., Freed and Burgmann, 2004). Nevertheless, this simplified approach using a 3-D viscoelastic model provides an improved representation of crustal velocities when compared to the elastic half-space model and the agreement with existing geodetic data is encouraging.

References

- Becker, T.W., J. Hardebeck, and G. Anderson, 2004, Constraints on fault slip rates of the southern California plate boundary from GPS velocity and stress inversions, *Geophys. J. Int.*, doi: 10.1111/j.1365-246.
- DeMets, C., Gordon, R.G., Argus, D.F., and Stein, S., 1994, Effect Of Recent Revisions to the Geomagnetic Reversal Time-Scale on Estimates of Current Plate Motions: *Geophysical Research Letters*, v. 21, p. 2191-2194.
- Freed, A.M., and R. Burgmann, 2004, Evidence of power-law flow in the Mojave desert mantle, *Nature*, 430, 548-551.
- Malservisi, R., K.P. Furlong, and T.H. Dixon, 2001, Influence of the earthquake cycle and lithospheric rheology on the dynamics of the eastern California shear zone, *Geophys. Res. Lett.*, 28, 2731-2734.
- Meade, B.J., and B.H. Hager, 2005, Block Models of Crustal Motion in Southern California Constrained by GPS Measurements, *J. Geophys. Res.*, 110, doi:10.1029/2004JB003209.
- Peltzer, G.P., P. Rosen, F. Rogez, and K. Hudnut, 1996, Postseismic rebound in fault step-overs caused by pore fluid flow, *Science*, 273, 1202-1204.
- Savage, J.C., and Prescott, W.H., 1978, Asthenosphere readjustment and the earthquake cycle: *Journal of Geophysical Research*, v. 83, p. 3369-3376.
- Smith, B., and Sandwell, D., 2003, Coulomb stress accumulation along the San Andreas Fault system: *Journal of Geophysical Research-Solid Earth*, v. 108.
- Smith, B.R., and Sandwell, D.T., 2006, A model of the earthquake cycle along the San Andreas Fault System for the past 1000 years: *Journal of Geophysical Research*, v. 111.
- Working Group on California Earthquake Probabilities, 1995, Seismic hazard in Southern California: Probable earthquakes, 1994 to 2024: *Bull. Seism. Soc. Am.*, v. 85, p. 379.
- Working Group on California Earthquake Probabilities, 1999, Earthquake Probabilities in the San Francisco Bay Region: 2000 to 2030 - A Summary of Findings.: USGS Open-File Report, p. 99-517.

TABLE DR2: FAULT SEGMENTS USED IN THE MODEL

Fault Segment	Slip Rate (mm/yr)	Locking Depth (km)
Imperial	40	4.1
Brawley SZ	25	4.4
Coachella	25	15.8
Palm Springs	25	21
San Bernardino	16	21
Superstition Hills	15	4.9
Borrego	15	9.2
Coyote Creek	15	9.2
Anza	15	9.2
San Jacinto Valley	12	9.2
San Jacinto Mountains	12	9.2
Laguna Salado	5	14.7
Elsinore	5	10.5
Helendale/Lenwood	2	10.5
Blackwater	5	10.5
ECSZ East	5	10.5
Owens Valley	4	10.5
Death Valley	5	10.5
Mojave	33	25.9
Carrizo	36	17.6
Cholame	36	8.9
Parkfield	36	10.2
Creeping	36	1.5

